Editors' Suggestion

Microfluidic slug transport on traveling-wave surface topographies by mechanowetting

Edwin de Jong [1], Jaap M. J. Den Toonder [2], and Patrick R. Onck [1,*]

[1] *Zernike Institute for Advanced Materials, University of Groningen, Groningen 9747 AG, The Netherlands*

[2] *Department of Mechanical Engineering and Institute for Complex Molecular Systems, Eindhoven University of Technology, Eindhoven 5600 MB, The Netherlands*

(Received 21 December 2018; accepted 11 May 2020; published 8 June 2020)

Nature often uses capillary forces to manipulate fluids, which has inspired scientists to develop new applications, such as in microfluidics and laboratory-on-a-chip systems. Here we present a method to transport fluids in microfluidic channels, by exploiting the capillary interaction of fluid interfaces with traveling surface waves, called mechanowetting. We found that the three-phase lines of fluid slugs dynamically attach to the crests of the waves, resulting in fluid velocities that are equal to the wave speed. By comparing this microfluidic slug flow to conventional peristaltic fluid propulsion, we demonstrate that fluid velocities can be reached that are one order of magnitude larger. We quantified the efficiency numerically and theoretically in terms of the generated pressure gradient using a closed channel and measured the evolution of the pressure distribution as the wave progresses. The method was shown to work for a very wide range of contact angles. We anticipate that our results will lead to new microfluidic applications based on switchable topography technology.

DOI: 10.1103/PhysRevFluids.5.063604

I. INTRODUCTION

Capillary forces are omnipresent in nature, governing fluid transport in a wide range of plants and animals [1]. Additionally, capillarity is very successfully employed in industry in, e.g., picoliter-droplet generation for inkjet printing, functional textiles for (self-)cleaning [2], and reduction of flow separation [3]. A major field that utilizes capillary properties is microfluidics [4], where fluid transport can be realized by applying wetting gradients induced by varying surface topographies or chemical composition [5–9] or by active manipulation of the interfacial energies by means of, e.g., electrowetting [10–13] and the Marangoni effect [14]. At the same time, more and more use is made of responsive materials and deforming topographies to manipulate fluids and solid objects, by exploiting time-dependent deformations that are externally controlled by, e.g., electric fields [15,16], light [17,18], and magnetic fields (e.g., by using artificial cilia [19,20]). Here we theoretically study a manifestation of capillary forces by surface deformation-controlled three-phase line motion, termed "mechanowetting," that is able to generate fluid transport that is remarkably fast, efficient, and versatile [21]. Because the three-phase line dynamically pins to traveling surface undulations, we show that the fluids in the channel can be transported. Such undulations can be generated by using moving light sources over light-responsive liquid crystal polymers [17,18,22–24], by alternating heating and cooling of responsive hydrogels embedded in elastic channel walls [25], or by utilizing vacuum-pressed thin polymer films on a moving structured belt [21].

*p.r.onck@rug.nl

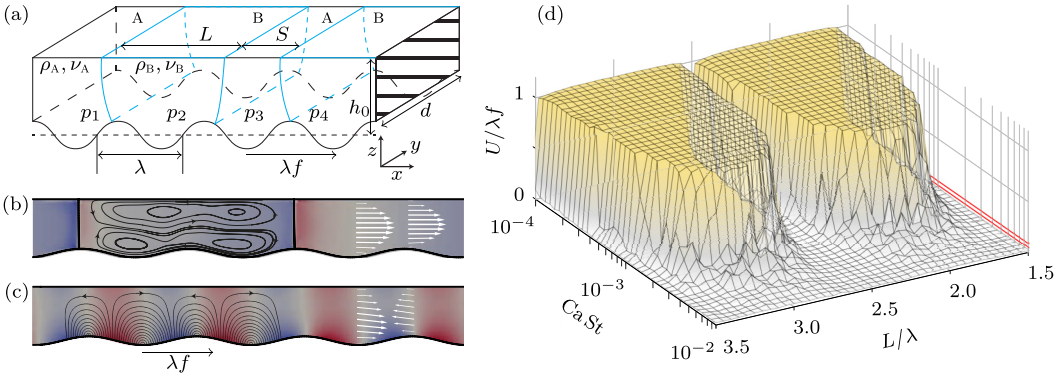

FIG. 1. (a) Schematics of the slug flow setup, highlighting the parameters in this study. For the closed-channel simulations, no-slip and no-flux boundary conditions are applied to the striped area at the right, while the boundary conditions at the right are traction-free. For the infinite-channel approach, the striped area is connected to the channel inlet at the left through periodic boundary conditions. (b) Streamlines (black lines, center-of-mass frame), velocity profile (white arrows, laboratory frame), and the pressure distribution (colors) of the infinite channel approach. Here $L = 200$ μm, $\theta_Y = 90°$. For an animation of the infinite channel simulation. (c) Streamlines (black lines, laboratory frame), velocity profile (white arrows, laboratory frame), and the pressure distribution (colors) of the peristaltic case, i.e., the wave topography applied to a channel filled with a single fluid. For the configurations shown in (b) and (c), the blue and red colors denote regions of low and high pressure, respectively, with absolute values that depend on the applied wave speed. Qualitatively the fields remain the same. (d) Steady-state slug speeds depending on slug length ratio L/λ and Ca St for the infinite-channel approach. $U/\lambda f = 1$ corresponds to fluid transport at the wave speed. Here $\theta_Y = 90°$, $\lambda = 100$ μm. The red lines correspond to the flow speed of single fluids (A and B) in the microchannel, subjected to the same traveling wave.

II. DIMENSIONAL ANALYSIS

We consider a microfluidic channel containing an incompressible fluid A (with density ρ_A and kinematic viscosity ν_A) in which a slug of the incompressible fluid B (ρ_B, ν_B) with size L is inserted [see Fig. 1(a)]. The interface between phases A and B has surface free energy γ_{AB}. The surface free energies of the interfaces between the solid S and the fluids A and B are γ_{SA} and γ_{SB}, respectively. The channel has an average height h_0 and out-of-plane depth d, and its bottom surface describes a transverse surface wave with wavelength λ, amplitude A, and frequency f. The three-phase lines at the surface of the waves cause the propulsion of the slug through mechanowetting [21]. Considering the typical dimensions of a microchannel and the corresponding microfluidic flow velocities, the slug flow is characterized by small Reynolds and capillary numbers, $\mathrm{Re} = Uh_0/\nu_A$ and $\mathrm{Ca} = \rho_A \nu_A U/\gamma_{AB}$, respectively, where U is the center-of-mass velocity of the slug. The relation between the applied traveling-wave speed λf and the slug's center-of-mass velocity U is best characterized by the Strouhal number, $\mathrm{St} = \lambda f/U$. Notably, the product CaSt can be studied, which can be interpreted as the wave capillary number, i.e., the capillary number of the flow if the fluid(s) exactly match the wave speed. The surface topography can be parametrized by the dimensionless ratios A/λ and A/h_0, and the slug geometry by the normalized slug length and spacing, L/λ and S/λ, respectively. The pressure in the channel is normalized by the surface free energy and channel height, ph_0/γ_{AB}. The surface-free energies of the solid-fluid and fluid-fluid interfaces are connected to the contact angle θ_Y by the Young equation, $\cos\theta_Y = (\gamma_{SB} - \gamma_{SA})/\gamma_{AB}$ [26]. The remaining parameters are the ratios between the fluid properties: the viscosity ratio ν_A/ν_B and density ratio ρ_A/ρ_B. We assume that there are no variations in the out-of-plane direction (y direction), so that the problem reduces to a two-dimensional analysis and d does not enter the problem. Unless specified otherwise, we fix the channel height at $h_0 = 50$ μm, the slug length at $L = 200$ μm, and three

of the dimensionless numbers at $A/\lambda = 1/25$, $\nu_A/\nu_B = 2.5$, $\rho_A/\rho_B = 0.8$. The latter parameters approximately represent an oil-water mixture.

III. NUMERICAL MODEL

We developed a two-phase computational fluid dynamics (CFD) model based on the finite-volume method to study fluid transport in the microchannel [21]. We solve the Navier-Stokes equations and the continuity equation, coupled with the smoothed continuous-surface-force formulation of the volume-of-fluid method (SCSF-VOF) [21,27–31]. The governing equations are given by

$$\frac{\partial \rho \boldsymbol{u}}{\partial t} + \boldsymbol{\nabla} \cdot (\rho \boldsymbol{u}\boldsymbol{u}) = -\boldsymbol{\nabla} p + \rho \boldsymbol{g} + \boldsymbol{\nabla} \cdot \{\nu[\boldsymbol{\nabla}\boldsymbol{u} + (\boldsymbol{\nabla}\boldsymbol{u})^{\top}]\} + \gamma_{AB}\kappa \boldsymbol{\nabla}\alpha, \tag{1}$$

$$\frac{\partial \rho}{\partial t} + \boldsymbol{\nabla} \cdot (\rho \boldsymbol{u}) = 0, \tag{2}$$

$$\frac{\partial \alpha}{\partial t} + \boldsymbol{\nabla} \cdot (\boldsymbol{u}\alpha) = -\boldsymbol{\nabla} \cdot [\boldsymbol{u}_r \alpha(1-\alpha)], \tag{3}$$

where $\boldsymbol{g}$ is the acceleration of gravity, γ_{AB} the surface free energy of the interface between fluids A and B, $\boldsymbol{u}$ the fluid velocity, $\kappa = -\boldsymbol{\nabla} \cdot \boldsymbol{n} = \boldsymbol{\nabla} \cdot (\boldsymbol{\nabla}\alpha/|\boldsymbol{\nabla}\alpha|)$ the interface curvature, and $0 \leqslant \alpha \leqslant 1$ an indicator field, which is 1 for fluid A and 0 for fluid B, with intermediate values indicating that an interface is located in the region. The last term at the right-hand side of Eq. (1) is the surface tension force. Equation (3) describes the evolution of the indicator field, where the term at the right-hand side compresses the field in the region of the interface, to ensure that the interface width stays within a small number of mesh points [32]. Here the compression velocity $\boldsymbol{u}_r = \boldsymbol{u}_A - \boldsymbol{u}_B$ represents the velocity difference between the two phases, a term that arises from defining the fluid velocity as a weighted average of the two phases A and B [33]. By calculating the interface curvature using a smoothed α field, we reduced the spurious velocities that appear near the interface in the VOF method [21,31]. By studying a static slug case as reference, we found that the spurious velocities at the interface are on the order of 5% of the obtained center-of-mass velocities. Finally, the fluid properties at each point in the field are implemented using the indicator α through (note that $0 \leqslant \alpha \leqslant 1$)

$$\nu = \alpha\nu_A + (1-\alpha)\nu_B, \quad \rho = \alpha\rho_A + (1-\alpha)\rho_B. \tag{4}$$

We employ two types of simulations, one for an infinite channel and one for a closed channel. For the infinite channel, we use periodic boundary conditions to connect the inlet and outlet of the channel, which results in an infinite array of slugs of size L that are a distance S apart. For the closed channel, at the left side of the slug, fluid A may freely enter or leave the domain, and at the right side the microfluidic channel is closed [see Fig. 1(a)].

For both types of simulations, on the top and bottom boundaries, we apply no-slip and no-flux boundary conditions. The contact angle θ_Y is implemented through the α field by computing the interface normal in terms of the contact angle and the boundary normal and tangent vector [28,34]:

$$\boldsymbol{n} = \boldsymbol{\nabla}\alpha/|\boldsymbol{\nabla}\alpha| = \boldsymbol{n}_{wall}\cos\theta_Y + \boldsymbol{t}_{wall}\sin\theta_Y. \tag{5}$$

At the top surface of the channel, for simplicity, we prescribe a contact angle for the fluid interface of $\theta_Y = 90^\circ$. The transverse traveling-wave surface topography is applied to the bottom wall and is modeled using a deforming boundary mesh, where we update the mesh boundary points using a height function and update the rest of the mesh accordingly to ensure mesh quality [29].

IV. NUMERICAL RESULTS

First, we analyze the infinite array of slugs by prescribing periodic boundary conditions. When the wave travels, the liquid-liquid interfaces adjust to the local inclination of the bottom surface topography. As a result, the interfaces become concave or convex, creating a Laplace pressure.

The CFD simulations show that the three-phase line dynamically pins to the crests of the surface wave, transporting the fluid slugs throughout the channel at the wave speed. The interfaces drive the flow and generate a constant pressure gradient along the length of the slugs (L) and the fluid compartments (S) that separate them [Fig. 1(b)]. The streamlines inside the slug (relative to the slug's center of mass reference frame) show a treadmilling flow profile consisting of a counterclockwise vortex at the top and a clockwise vortex at the bottom. The velocity vectors (represented by the white arrows, plotted in the laboratory frame) show that the fluid velocity is positive throughout the whole channel. This compares positively to the situation where no slugs are present [i.e., conventional peristaltic flow; see Fig. 1(c)]. Here, although the average fluid velocity is positive (typically, $0.01 < U/\lambda f < 0.1$), the streamlines and velocity vectors (both plotted in the laboratory frame) show a strong reflux profile which prevents high fluid throughput. Analysis at relatively high wave speeds of the microfluidic slug flow [see Fig. 1(d), which shows the steady-state slug speed $U/\lambda f$ as a function of CaSt and slug length L/λ] demonstrates that, at integer values of L/λ, the effectiveness of the transport mechanism ($U/\lambda f = 1$) is maintained for a large range of applied wave speeds (i.e., CaSt $\leqslant 2 \times 10^{-3}$). For reference, two fluids of $\rho_{\mathrm{A}} = 10^3\ \mathrm{kg\,m^{-3}}$, $\nu_{\mathrm{A}} = 10^{-6}\ \mathrm{m^2\,s^{-1}}$, $\rho_{\mathrm{B}} = 8 \times 10^2\ \mathrm{kg\,m^{-3}}$, $\nu_{\mathrm{A}} = 2.5 \times 10^{-6}\ \mathrm{m^2\,s^{-1}}$, and $\gamma_{\mathrm{AB}} = 0.05\ \mathrm{mN\,m^{-1}}$ were used in the simulations, such that CaSt $= 10^{-3}$ yields slug velocities of approximately $U = \lambda f \approx 2\ \mathrm{cm\,s^{-1}}$. We compare the two-phase slug speed with the regular one-phase flow speed of a fluid-filled channel subject to the same transverse wave. The fluid will then be transported in a peristaltic manner, reaching speeds that, however, are an order of magnitude smaller than the slug speeds [i.e., for fluid A, $U/\lambda f = 0.028$ and for fluid B, $U/\lambda f = 0.070$, represented by the solid red lines in the back of Fig. 1(d)]. It is observed that at integer values of L/λ, a maximum slug speed is reached. For larger wave speeds, the slugs speed drops to zero, indicating that the capillary forces are not sufficient to drive the slug at the wave speed, which is due to the enhanced viscous drag at the channel walls. In addition, at semi-integer values of L/λ, the efficiency drops considerably. This will be further discussed in the next sections.

Next, we analyze the slug in a closed channel. In contrast to the infinite-channel approach, the slug is now kept in place by the constant-volume constraint. A single simulation for $L/\lambda = 2$ [Fig. 2(a)–2(d)] shows that the pressures in the three regions p_1, p_2, and p_3 are uniform [in contrast with the infinite channel, where a small pressure gradient was observed in each region; see Fig. 1(b)]. The reference pressure p_1 is always zero, due to the open boundary at the left, while the pressures p_2 and p_3 can be either positive [when the surface wave attains the position shown in Fig. 2(b)], negative [for the situation in Fig. 2(d)], or zero everywhere [when the two slug interfaces are both located at a valley or peak of the wave, Fig. 2(c)]. Because the pressure difference $\Delta p = p_3 - p_1$ is generated by the interfaces of the slug, its magnitude can be used as a measure for the transport performance of the slug that would take place were the channel not closed (i.e., the infinite channel case described above). In a second simulation [Fig. 2(f) and 2(g)] for $L/\lambda = 1.5$, we see that the pressure jumps across the interfaces are of opposite sign, effectively resulting in $p_3 \approx p_1$, and thus no pressure build up can be generated for this slug size-wavelength combination. Further inspection reveals that the maximum pressure build up is largest near integer values of L/λ [Fig. 2(e)]. The integer ratios correspond to the situation in which both slug interfaces are concave (viewed from left to right), i.e., both interfaces contribute to an increased Laplace pressure to the right consisting of two pressure jumps over the two interfaces [see Fig. 2(b)]. For noninteger values of L/λ, the slug interfaces can be either concave or convex, which results in a pressure jump of opposite sign over the two separate interfaces and thus partially canceling the pressure build up. The optimal values for L/λ shift when the contact angle θ_{Y} changes due to the fact that the local inclination of the interface changes when changing the contact angle, leading to a different interface curvature and thus Laplace pressure (see Fig. 3). In addition, the study clearly shows an optimal pressure build up at $\theta_{\mathrm{Y}} = 90^\circ$, for integer values of L/λ.

If there are two or more slugs in the channel, their distance can affect the transport efficiency as well. To analyze this, we modeled two slugs in a closed channel ($\theta_{\mathrm{Y}} = 90^\circ$) and measured the pressure difference between the left and right sides of the channel [i.e., $\Delta p = p_5 - p_1$; see Figs. 4(a)

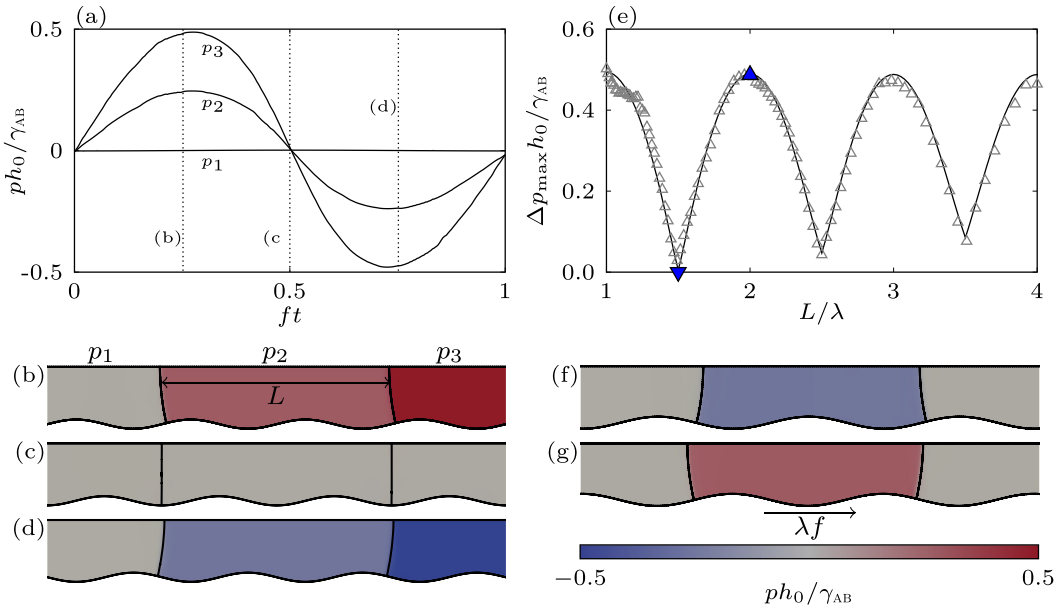

FIG. 2. Pressures in the closed-channel approach to quantify the efficiency of the (a) steady-state pressure evolution as a function of time corresponding to the three regions indicated in (b)–(d). The conformations at three different instances indicated by the dashed lines are shown in (b)–(d). Here $L = 200$ μm, $\lambda = 100$ μm. (b)–(d) Pressure distributions at times denoted in (a). (e) The maximum pressure built up on the right side of the slug related to the slug length for the closed-channel simulations (triangles) and corresponding theory [Eq. (11), solid line]. The two filled upward-pointing and downward-pointing triangles correspond to the situations in (b) and (g), respectively. (f), (g) Pressure distributions for $L = 200$ μm, $\lambda = 133$ μm. Here the curvatures of the two interfaces create a pressure jump of opposite sign, resulting in $p_1 = p_3$ at all times and no pressure build up occurs, while p_2 is fluctuating between the situations shown in (f) and (g).

and 4(b)]. The influence of the slug spacing S was numerically evaluated for $2.4 \leqslant L/\lambda \leqslant 3.6$ and is shown in Fig. 4(c). The results show a clear periodicity of 1 for both S/λ and L/λ (identical to the one-slug situation for $\theta_Y = 90°$). This means that, in a similar fashion as the slug length

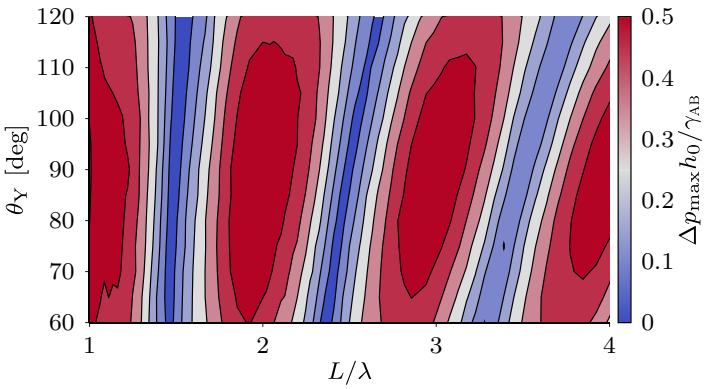

FIG. 3. Numerical results for the closed-channel approach. Contour plot showing the dependence of the generated maximum pressure difference Δp_{max} on the normalized slug length and the contact angle θ_Y for the closed channel (see Fig. 2). Here $L = 200$ μm and the wavelength λ was varied.

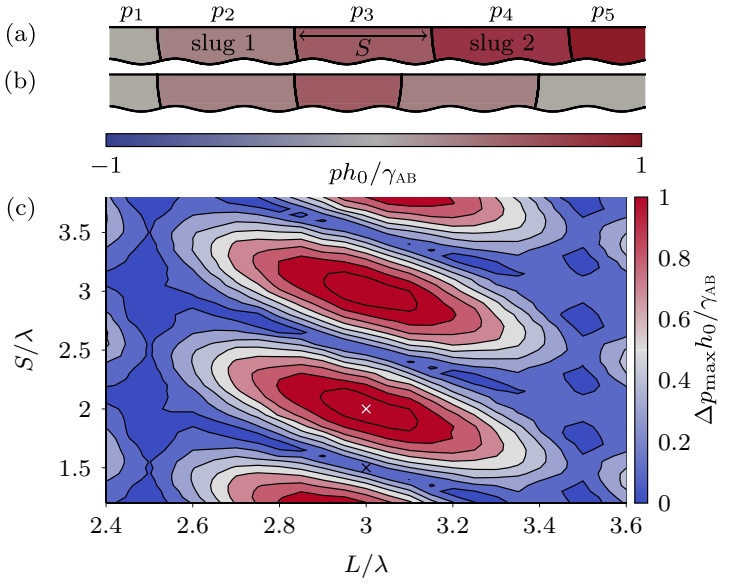

FIG. 4. Numerical results for the closed-channel, containing two slugs. (a) Numerical dual-slug simulation in a closed channel for $\theta_Y = 90°$. Here $L = S = 200$ μm. The wavelength λ and slug spacing S were varied. Because $S/\lambda = 2$, the slugs are both contributing constructively in the pressure build up. (b) Dual-slug simulation in a closed channel for $S/\lambda = 1.5$. The pressure that was built up by two consecutive slugs destructively interferes, which results in an end pressure of $p_5 \approx p_1$, where p_5 is the pressure at the right side of the channel and p_1 at the left (as indicated in the figure). (c) Normalized maximum pressure difference ($\Delta p = p_5 - p_1$) for the two-slug case, as a function of channel parameters L/λ and S/λ. The crosses at $S/\lambda = 1.5, 2$ correspond to the snapshots shown in (a) and (b), respectively.

L, the slug separation-wavelength ratio, i.e., S/λ, must be an integer, to maximally transport the fluids. Moreover, the magnitude of the normalized pressure difference has doubled in the dual-slug simulations [see Fig. 4(c) as compared to Fig. 3]. This indicates that the driving force scales one-to-one with the number of slugs in the channel.

V. THEORETICAL MODEL AND RESULTS

In order to explain the generated numerical data, we carried out a theoretical analysis to calculate the build up of Laplace pressure. The fluid interfaces are modeled as circular segments, and their curvature can be written by using the radius of the circular cap, $\kappa = R^{-1}$. Because the Reynolds number is very low, we use a quasistatic approach, i.e., the dynamic (inertial) effects are neglected. Consequently, the instantaneous surface height profile can be written as

$$z(\varphi) = A\cos(2\pi\varphi), \tag{6}$$

where $\varphi \equiv x/\lambda$. The vertical distance from the three-phase line to the top of the channel [see Fig. 1(a)] is given by

$$h(\varphi) = h_0 - z(\varphi), \tag{7}$$

where h_0 is the mean height of the channel. The curvature of a single interface can be expressed as

$$\frac{1}{R(\varphi)} = \frac{\sin[\beta(\varphi)]}{h(\varphi)}, \tag{8}$$

where the angle

$$\beta(\varphi) \equiv \arctan\left[-\frac{2\pi A}{\lambda}\sin(2\pi\varphi)\right] - (-1)^n\left(\theta_Y - \frac{\pi}{2}\right) \tag{9}$$

expresses the local inclination of the surface at the three-phase line for a sinusoidal surface, with $n = 1, 2, \ldots$ accounting for the fact that the contact angle either increases or decreases the interface curvature when crossing an interface A → B or B → A. The location of the second interface (B → A at φ_2) can be calculated from the location of the first interface φ_1 and the constant slug volume constraint, by solving the expression

$$\begin{aligned} Lh_0 = {} & \frac{R_1^2}{4}[2\beta_1 - \sin(2\beta_1)] - \frac{R_2^2}{4}[2\beta_2 - \sin(2\beta_2)] + \lambda h_0(\varphi_2 - \varphi_1) \\ & - \frac{A\lambda}{2\pi}[\sin(2\pi\varphi_2) - \sin(2\pi\varphi_1)] \end{aligned} \tag{10}$$

using a root-finding algorithm. Here the substitutions $R_i = R(\varphi_i)$ and $\beta_i = \beta(\varphi_i)$ were made. The four terms on the right-hand side of Eq. (10) represent (i) the increase in volume due to the curvature of the left interface, (ii) the decrease in volume due to the curvature of the right interface, (iii) the volume of the bulk of the slug, and (iv) the correction of the sinusoidal shape of the bottom of the microchannel, respectively. From Eq. (10), φ_2 is obtained for all values of $\varphi_1 \in [0, 1]$. The obtained parameter set, φ_1 and φ_2, is used to calculate the Laplace pressure by using Eqs. (7) and (8):

$$\Delta p = \gamma_{AB}\left(R_1^{-1} + R_2^{-1}\right). \tag{11}$$

This equation gives an expression for the pressure difference in terms of the fluid and channel parameters, while the channel surface deforms with time. The maximum value of this pressure difference is plotted together with the numerical data for $\theta_Y = 90^\circ$ and $L = 200$ μm in Fig. 2(e), showing excellent agreement. Additionally, the θ_Y and S/λ dependencies are correctly reproduced by the theory, as can be seen by comparing Fig. 5(a) and 5(b) with Fig. 3 and Fig. 4(c), respectively. Here, to obtain the theoretical data for S/λ, the model was extended in a straightforward manner to account for multiple slugs, by incorporating higher values for n in Eq. (9).

VI. DISCUSSION AND CONCLUSIONS

A recent experimental study suggests that systems that rely on surface energy minimization of the fluid end caps require completely wetting liquids, $\theta_Y = 0^\circ$ [18]. However, our numerical and theoretical analyses show that the currently proposed mechanism works for a large range of contact angles, i.e., the partial wetting regime ($0 < \theta_Y < 180^\circ$), showing a theoretical optimum at $\theta_Y = 90^\circ$. The underlying physical mechanism of the slug-driven flow in microfluidic channels studied here is similar in nature to that of single-droplet transport on free surfaces in air [21]. We termed this "mechanowetting," as it is driven by the dynamic three-phase line pinning to mechanically deforming surfaces. It should thus be noted that not only does the current mechanowetting propulsion mechanism hold for two distinct liquids such as oil and water, but that it is also operative for liquid and gas combinations such as water (or glycol) and air.

The measured performance can be sensitive to small changes in the contact angle, but this effect can be easily compensated for by adjusting the slug size L and spacing S, following the data presented in this paper [see, e.g., Fig. 4(c)]. Other methods that utilize transverse waves, such as surface acoustic waves (SAWs), require complex integrated electrodes and are performed at the MHz-frequency regime and therefore can cause rapid heating of the substrate [35,36]. Although SAWs and mechanowetting are both based on traveling surface waves, the physical mechanisms are different and operate in widely different frequency regimes. In SAWs, high-frequency distortion of the three-phase line generates capillary waves along the interface, while in mechanowetting, the

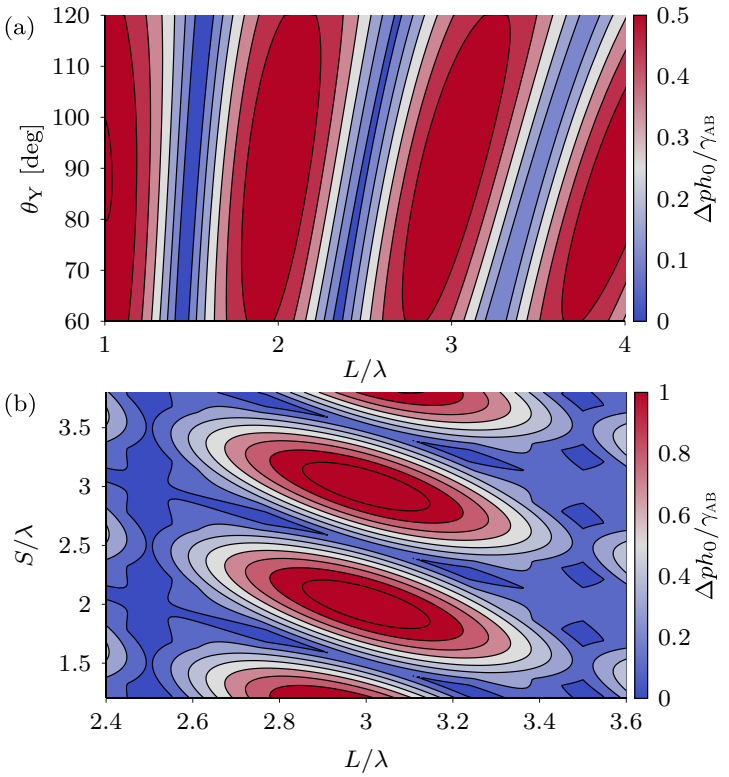

FIG. 5. Theoretical model for the closed-channel configuration based on Eq. (11), showing the θ_Y dependence (a) and the S/λ dependence (b) of the generated maximum pressure differences, showing excellent agreement with the CFD data of Fig. 3 and Fig. 4(c).

deformation of the solid surface distorts the contact angle and drives the three-phase line along with the wave.

By making simplifying assumptions, we aim to gain insights in the limiting behavior of Eq. (11). By assuming $\theta_Y = 90^\circ$ and $L = m\lambda$ (where m is an integer), we find that Eq. (10) is satisfied when $\varphi_2 = \varphi_1 + m$, which at the same time implies that $R_1 = R_2$. Additionally, Eq. (11) is maximized when R_1 is minimized. This can be easily derived from Eq. (8), showing that this is the case when $\varphi_1 = -1/4 + k$ (where k is an integer). By substituting these expressions in Eq. (11), we obtain an approximation that reveals the dependence of the pressure difference on the geometric parameters of the system:

$$\Delta p_{\max} = \frac{2\gamma_{AB}}{h_0} \frac{\frac{2\pi A}{\lambda}}{\sqrt{\left(\frac{2\pi A}{\lambda}\right)^2 + 1}} \approx \begin{cases} \frac{2\gamma_{AB}}{h_0}\frac{2\pi A}{\lambda} & \left[\frac{A}{\lambda} \ll 1\right] \\ \frac{2\gamma_{AB}}{h_0} & \left[\frac{A}{\lambda} \gg 1\right] \end{cases}. \tag{12}$$

Hence, the pressure difference is inversely proportional to the mean channel height h_0, and it is proportional to the surface wave amplitude A for small A, whereas it is independent of A in the limit of large A. Equation (12) also shows that the driving force scales linearly with the surface tension γ_{AB}, so that fluid combinations (such as water-air) with higher surface tension increases the maximum pressure that can be generated.

In order to transport a single slug, it is obviously required only to have wavelike protrusions near the three-phase lines of the slug itself. However, the wave-type surface topography has some advantages, especially when multiple slugs are put inside the channel at the correct spacing. By

comparing the pressures from Fig. 4(a) and Fig. 2(b), we observe that the built-up pressure gradient doubles when adding a second slug of fluid B, i.e., the pressure gradient scales linearly with the number of slugs. When designed accordingly and the number of slugs is increased even further, the slugs will work collectively as a pump to displace fluids throughout the whole system.

All in all, we have theoretically and numerically explored a microfluidic slug transport mechanism based on traveling-wave surface topographies. By exploiting the capillary properties of the system, fluid velocities can be generated that are equal to the applied wave speed. The generated speeds are an order of magnitude larger than the peristaltic flow speeds of single-phase fluids and do not require fully wetting liquids. The slug transport efficiency was quantified by analyzing the pressure build up in closed microchannels, and its dependence on the contact angle θ_Y, the slug length L, and the slug spacing S (relative to the wavelength λ) was fully captured in closed-form expressions. We expect our approach of slug transport to lead to new applications based on three-phase line manipulation by switchable surface topographies.

ACKNOWLEDGMENT

This work was supported by NWO-TTW under Project No. 12826, "Dynaclean".

[1] D. Ishii, H. Horiguchi, Y. Hirai, H. Yabu, Y. Matsuo, K. Ijiro, K. Tsujii, T. Shimozawa, and T. Hariyama, Water transport mechanism through open capillaries analyzed by direct surface modifications on biological surfaces, Sci. Rep. **3**, 1 (2013).

[2] D. Li and Z. Guo, Versatile superamphiphobic cotton fabrics fabricated by coating with SiO_2/FOTS, Appl. Surf. Sci. **426**, 271 (2017).

[3] C. Duez, C. Ybert, C. Clanet, and L. Bocquet, Wetting Controls Separation of Inertial Flows from Solid Surfaces, Phys. Rev. Lett. **104**, 084503 (2010).

[4] G. M. Whitesides, The origins and the future of microfluidics, Nature (London) **442**, 368 (2006).

[5] N. Moradi, F. Varnik, and I. Steinbach, Roughness-gradient-induced spontaneous motion of droplets on hydrophobic surfaces: A lattice Boltzmann study, Europhys. Lett. **89**, 26006 (2010).

[6] F. Varnik, M. Gross, N. Moradi, G. Zikos, P. Uhlmann, P. Müller-Buschbaum, D. Magerl, D. Raabe, I. Steinbach, and M. Stamm, Stability and dynamics of droplets on patterned substrates: Insights from experiments and lattice Boltzmann simulations, J. Phys.: Condens. Matter **23**, 184112 (2011).

[7] J.-J. Huang, H. Huang, and X. Wang, Numerical study of drop motion on a surface with stepwise wettability gradient and contact angle hysteresis, Phys. Fluids **26**, 062101 (2014).

[8] C. Lv, C. Chen, Y.-C. Chuang, F.-G. Tseng, Y. Yin, F. Grey, and Q. Zheng, Substrate Curvature Gradient Drives Rapid Droplet Motion, Phys. Rev. Lett. **113**, 026101 (2014).

[9] J. Bico and D. Quéré, Self-propelling slugs, J. Fluid Mech. **467**, 101 (2002).

[10] A. M. Pit, M. H. G. Duits, and F. Mugele, Droplet manipulations in two phase flow microfluidics, Micromachines **6**, 1768 (2015).

[11] G. Van der Veen and W. Prins, Photomechanical energy conversion in a polymer membrane, Nature (London) **230**, 70 (1971).

[12] M. G. Pollack, R. B. Fair, and A. D. Shenderov, Electrowetting-based actuation of liquid droplets for microfluidic applications, Appl. Phys. Lett. **77**, 1725 (2000).

[13] S. W. Walker, B. Shapiro, and R. H. Nochetto, Electrowetting with contact line pinning: Computational modelling comparisons with experiments, Phys. Fluids **21**, 102103 (2009).

[14] L. Zhang, Y. Yuan, X. Qiu, T. Zhang, Q. Chen, and X. Huang, Marangoni effect-driven motion of miniature robots and generation of electricity on water, Langmuir **33**, 12609 (2017).

[15] J. Xie, J. Shih, Q. Lin, B. Yang, and Y.-C. Tai, Surface micromachined electrostatically actuated micro peristaltic pump, Lab Chip **4**, 495 (2004).

[16] T. Wang, M. Farajollahi, Y. S. Choi, I.-T. Lin, J. E. Marshall, N. M. Thompson, S. Kar-Narayan, J. D. W. Madden, and S. K. Smoukov, Electroactive polymers for sensing, Interface Focus **6**, 20160026 (2016).

[17] D. Liu, L. Liu, P. R. Onck, and D. J. Broer, Reverse switching of surface roughness in a self-organized polydomain liquid crystal coating, Proc. Natl. Acad. Sci. USA **112**, 3880 (2015).
[18] J.-A. Lv, Y. Liu, J. Wei, E. Chen, L. Qin, and Y. Yu, Photocontrol of fluid slugs in liquid crystal polymer microactuators, Nature (London) **537**, 179 (2016).
[19] S. N. Khaderi, C. B. Craus, J. Hussong, N. Schorr, J. Belardi, J. Westerweel, O. Prucker, J. Ruhe, J. M. J. den Toonder, and P. R. Onck, Magnetically-actuated artificial cilia for microfluidic propulsion, Lab Chip **11**, 2002 (2011).
[20] J. M. J. den Toonder and P. R. Onck, Microfluidic manipulation with artificial/bioinspired cilia, Trends Biotechnol. **31**, 85 (2013).
[21] E. de Jong, Y. Wang, J. M. J. den Toonder, and P. R. Onck, Climbing droplets driven by mechanowetting on transverse waves, Sci. Adv. **5**, eaaw0914 (2019).
[22] T. J. White and D. J. Broer, Programmable and adaptive mechanics with liquid crystal polymer networks and elastomers, Nat. Mater. **14**, 1087 (2015).
[23] S. Palagi, A. G. Mark, S. Y. Reigh, K. Melde, T. Qiu, H. Zeng, C. Parmeggiani, D. Martella, A. Sanchez-Castillo, N. Kapernaum, *et al.*, Structured light enables biomimetic swimming and versatile locomotion of photoresponsive soft microrobots, Nat. Mater. **15**, 647 (2016).
[24] L. Liu and P. R. Onck, Enhanced Deformation of Azobenzene-Modified Liquid Crystal Polymers Under Dual Wavelength Exposure: A Photophysical Model, Phys. Rev. Lett. **119**, 057801 (2017).
[25] V. Nistor, J. Cannell, J. Gregory, and L. Yeghiazarian, Stimuli-responsive cylindrical hydrogels mimic intestinal peristalsis to propel a solid object, Soft Matter **12**, 3582 (2016).
[26] T. Young, An essay on the cohesion of fluids, Philos. Trans. R. Soc. London **95**, 65 (1805).
[27] C. W Hirt and B. D Nichols, Volume of fluid (VOF) method for the dynamics of free boundaries, J. Comput. Phys. **39**, 201 (1981).
[28] J. U Brackbill, D. B Kothe, and C. Zemach, A continuum method for modeling surface tension, J. Comput. Phys. **100**, 335 (1992).
[29] H. Jasak, Error analysis and estimation in the Finite Volume method with applications to fluid flows, Ph.D. thesis, Imperial College London (1996).
[30] O. Ubbink, Numerical prediction of two fluid systems with sharp interfaces, Ph.D. thesis, Imperial College London (1997).
[31] A. Q. Raeini, M. J. Blunt, and B. Bijeljic, Modelling two-phase flow in porous media at the pore scale using the volume-of-fluid method, J. Comput. Phys. **231**, 5653 (2012).
[32] E. Berberović, N. P. van Hinsberg, S. Jakirlić, I. V. Roisman, and C. Tropea, Drop impact onto a liquid layer of finite thickness: Dynamics of the cavity evolution, Phys. Rev. E **79**, 036306 (2009).
[33] O. Ubbink and R. I. Issa, A method for capturing sharp fluid interfaces on arbitrary meshes, J. Comput. Phys. **153**, 26 (1999).
[34] M. Wörner, Numerical modeling of multiphase flows in microfluidics and micro process engineering: A review of methods and applications, Microfluid. Nanofluid. **12**, 841 (2012).
[35] C.-G. Yang, Z.-R. Xu, and J.-H. Wang, Manipulation of droplets in microfluidic systems, Trends Anal. Chem. **29**, 141 (2010).
[36] B. H. Ha, K. S. Lee, G. Destgeer, J. Park, J. S. Choung, J. H. Jung, J. H. Shin, and H. J. Sung, Acoustothermal heating of polydimethylsiloxane microfluidic system, Sci. Rep. **5**, 11851 (2015).